A well-calibrated ocean algorithm for special sensor microwave / imager

Frank J. Wentz

Remote Sensing Systems, Santa Rosa, California

Abstract. I describe an algorithm for retrieving geophysical parameters over the ocean from special sensor microwave / imager (SSM/I) observations. This algorithm is based on a model for the brightness temperature T_B of the ocean and intervening atmosphere. The retrieved parameters are the near-surface wind speed W, the columnar water vapor V, the columnar cloud liquid water L, and the line-of-sight wind W_{LS}. I restrict my analysis to ocean scenes free of rain, and when the algorithm detects rain, the retrievals are discarded. The model and algorithm are precisely calibrated using a very large in situ database containing 37,650 SSM/I overpasses of buoys and 35,108 overpasses of radiosonde sites. A detailed error analysis indicates that the T_B model rms accuracy is between 0.5 and 1 K and that the rms retrieval accuracies for wind, vapor, and cloud are 0.9 ms^{-1}, 1.2 mm, and 0.025 mm, respectively. The error in specifying the cloud temperature will introduce an additional 10% error in the cloud water retrieval. The spatial resolution for these accuracies is 50 km. The systematic errors in the retrievals are smaller than the rms errors, being about 0.3 ms^{-1}, 0.6 mm, and 0.005 mm for W, V, and L, respectively. The one exception is the systematic error in wind speed of -1.0 ms^{-1} that occurs for observations within $\pm20°$ of upwind. The inclusion of the line-of-sight wind W_{LS} in the retrieval significantly reduces the error in wind speed due to wind direction variations. The wind error for upwind observations is reduced from -3.0 to -1.0 ms^{-1}. Finally, I find a small signal in the 19-GHz, horizontal polarization (h$_{pol}$) T_B residual ΔT_{BH} that is related to the effective air pressure of the water vapor profile. This information may be of some use in specifying the vertical distribution of water vapor.

1. Introduction

With the advent of well-calibrated satellite microwave radiometers, it is now possible to obtain long time series of geophysical parameters that are important for studying the global hydrologic cycle and the Earth's radiation budget. Over the world's oceans these radiometers have the capability to simultaneously measure profiles of air temperature and the three phases of atmospheric water (vapor, liquid, and ice). In addition, surface parameters such as the near-surface wind speed, the sea-surface temperature, and sea ice type and concentration can be retrieved. A wide variety of hydrological and radiative processes can be studied with these measurements, including air-sea and air-ice interactions (i.e., the latent and sensible heat fluxes, freshwater flux, and surface stress) and the effect of clouds on radiative fluxes. The microwave radiometer is truly a unique and valuable tool for studying our planet.

In this paper I focus on the problem of retrieving geophysical parameters over the world's oceans from the observations taken by the special sensor microwave imager (SSM/I) [Hollinger et al., 1987]. The SSM/I is flown by the Defense Meteorological Satellite Program (DMSP) on two operational polar orbiting platforms. The first in the series of seven SSM/I's was launched in June 1987, and the SSM/I series will

probably continue through about the year 2000, at which time it will be replaced by a combined imager/sounder called SSM/IS. Thus there is the opportunity to obtain a 13-year global time series of geophysical products, which can then be further extended with the SSM/IS observations.

The SSM/I operates at the following four frequencies: 19.35, 22.235, 37, and 85.5 GHz. With these channels it is possible to retrieve three important geophysical parameters over the ocean: near-surface wind speed W (meters per second), columnar water vapor V (millimeters), and columnar cloud liquid water L (millimeters). Rainfall can also be inferred, but in this paper I restrict my investigation to ocean scenes free of rain. In the absence of rain there is a relatively simple and unique relationship between the ocean brightness temperature T_B measured by SSM/I and W, V, and L. The occurrence of rain adds considerable complexity to the problem that, for now, I want to avoid.

Potentially, W, V, and L can be retrieved to a high degree of accuracy because of the unique relationship between T_B and (W,V,L). This relationship is given by the radiative transfer equation (RTE) for a nonraining atmosphere bounded at the bottom by a rough sea surface. It has been shown that this RTE can be approximated by a relatively simple closed-form expression (i.e., no integrals), which is called the T_B model function [Wentz, 1983]. The retrieval of (W,V,L) is accomplished by varying these parameters until the T_B model function matches the SSM/I observations. Thus the accuracy of (W,V,L) depends on the accuracy of the T_B model. In order to obtain the highest possible retrieval accuracies, the T_B model must include the effects of all the relevant parameters in the RTE and the T_B model must be precisely calibrated. The

complete parameterization of the T_B model function and its subsequent precision calibration are the subject of this paper.

The paper begins with a description of the SSM/I sensor and observations. I then discuss the parameterization of the T_B model. There are the three primary parameters, W, V, and L, and four secondary parameters, sea-surface temperature T_S (kelvins), effective atmospheric temperature T_E (kelvins), effective atmospheric pressure P (millibars) of the water vapor column, and wind direction ϕ. The dependence of T_B on these secondary parameters is weak relative to the primary parameters. However, these secondary dependencies are still significant and must be taken into account. Section 3 discusses the statistical relationships derived from climatology that are used to specify T_S, and T_E, and P.

Wind direction is too variable to be specified via climatology, and hence I included it as a fourth retrieval parameter in addition to W, V, and L. Wind direction enters the T_B model in terms of the line-of-sight wind component W_{LS}, which is the component of the wind vector along the SSM/I observation direction. The inclusion of W_{LS} as a fourth retrieval has two benefits. First, it reduces the retrieval error in the other parameters (particularly W), and second, it provides new information on wind direction over the oceans.

The retrieval algorithm is discussed in section 4. For each SSM/I pixel the algorithm finds the value for (W,V,L,W_{LS}) that, when substituted into the T_B model, produces T_B values that equal the SSM/I observations at 19-GHz v_{pol}, 22-GHz v_{pol}, 37-GHz v_{pol}, and 37-GHz h_{pol}. The T_B model is quasi-linear in terms of the four parameters, and hence the retrieval involves solving four equations in four unknowns. The complete formulation for the T_B model is given in section 5.

Sections 6 and 7 describe the very large buoy and radiosonde data sets that are used to calibrate the model and retrieval algorithm. Global buoy and radiosonde observations are collected for the 4-year period from 1987 through 1990. There are 66 buoy sites and 55 radiosonde sites. These in situ measurements are collocated with SSM/I overpasses. The collocation procedure yields a total of 37,650 SSM/I overpasses of buoys and 35,108 overpasses of radiosonde sites.

The derivation of the atmospheric coefficients in the T_B model is described in section 8. Theoretical brightness temperatures are computed from the radiosonde observations using the complete integral formulation of the RTE. These theoretical T_B values are used to calculate the atmospheric coefficients in the T_B model. The retrieval errors due to approximations in the atmospheric part of the T_B model are determined by doing simulations in which the RTE T_B values serve as input to the retrieval algorithm. Section 8 also discusses the effect of air pressure variations on the retrievals.

The calibration of the T_B model (and hence the retrieval algorithm) via an inverse modeling technique is discussed in section 9. The calibration is done by varying the coefficients in the T_B model so that the W and V retrievals match buoy and radiosonde observations. Furthermore, histograms of the L retrievals are required to satisfy a number of statistical constraints. In all, the W, V, and L retrievals are required to meet 19 statistical conditions. This type of calibration is called inverse modeling because the derivation of the model's coefficients is based on the outputs of the model's inverse (i.e., the retrieval algorithm).

Section 10 discusses the retrieval of W_{LS} and the wind speed error due to variations in wind direction. I conclude with a complete error analysis. An error budget table shows how the T_B modeling error, the radiometer noise, and the SSM/I in situ spatial-temporal sampling error all contribute to the total observed rms variation in the retrievals. On the basis of this error analysis, I estimate the accuracy of the T_B model and the geophysical retrievals.

Via a competitive peer review, NASA has selected the algorithm described herein for producing the scanning multi-channel microwave radiometer (SMMR)-SSM/I Pathfinder Data Set. This data set will be a 20-year time series of geophysical parameters, which will be broadly distributed to the research community.

2. Description of the SSM/I

The analysis herein is based on the 1987-1990 observations of the first SSM/I that flew on the DMSP F08 spacecraft [Hollinger et al., 1987]. The orbit for F08 spacecraft is near-circular, Sun-synchronous, and near-polar, with an inclination of 98.8°. The altitude is 860 ± 25 km, and the orbital period is 102 min. The variation in altitude is due to the eccentricity of the orbit and the oblateness of the Earth. The local time for the ascending equatorial crossing for F08 is 0615 LT.

The SSM/I sensor consists of seven separate total-power radiometers sharing a common feedhorn. These seven radiometers take dual-polarization measurements at 19.35, 37.0, and 85.5 GHz, and just a vertical-polarization measurement at 22.235 GHz. The SSM/I uses an offset parabolic reflector of dimensions 61 by 66 cm to collect the microwave radiation. The reflector focuses the radiation into the corrugated, broadband, seven-port feedhorn. The reflector and feedhorn spin as a unit about the nadir axis. The rotation period is 1.9 s. A cold-space reflector and a hot reference load are attached to the spin axis and do not rotate. The rotating feedhorn observes the fixed cold reflector and hot load once each scan. In this way, calibration observations are taken every scan.

Earth observations are taken during a 102.4° segment of the rotation. The 102.4° arc is centered on the spacecraft subtrack and corresponds to a 1400-km-wide swath on the Earth's surface. The 1400-km swath and the orbit inclination of 98.8° provide complete coverage of the Earth in 2 to 3 days, except for two small circular sectors of 2.4° centered on the north and south poles. The nadir angle for the Earth-viewing reflector is 45°, which results in an Earth incidence angle of 53.4° ± 0.25°. The lower-frequency channels (19, 22, and 37 GHz) are sampled so that the pixel spacing is 25 km, and the 85-GHz channels are sampled at a 12.5-km pixel spacing.

The SSM/I measures the intensity of radiation coming from the Earth-viewing reflector. The Rayleigh-Jeans approximation [Eisberg, 1961] expresses this intensity in terms of a temperature, called the antenna temperature T_A. For SSM/I the antenna temperature is approximated by

$$T_{AIP} = G_{IPV} T_{BIV} + G_{IPH} T_{BIH} + G_{IPO} T_{BC} \qquad (1)$$

where subscripts I and P denote the frequency and polarization, respectively, and T_{BIV} and T_{BIH} are the v_{pol} and h_{pol} Earth brightness temperatures. T_{BC} is the cosmic background radiation equaling 2.7 K. The G factors are the antenna pattern coefficients that account for the antenna spillover and the cross-polarization leakage. The derivation of approximation (1) and the values for the G coefficients are given by Wentz [1991].

The antenna temperatures are averaged to a common spatial resolution. The half-power beam widths of the SSM/I

footprints on the Earth are 56, 44, and 32 km for the 19-, 22-, and 37-GHz channels, respectively, and the centers of these footprints are coincident. Hence a 37-GHz observation only sees 33% of the area sampled by the 19-GHz channel. In order to obtain accurate retrievals, it is necessary that all channels see the same ocean area. This is accomplished by averaging the 22- and 37-GHz observations down to the lower resolution of the 19-GHz channel using the following equation:

$$\bar{T}_{AIJ} = \sum_{i=I-1}^{I+1} \sum_{j=J-1}^{J+1} w_{ij} T_{Aij} \qquad (2)$$

in which T_{Aij} is antenna temperature (either at 22 or 37 GHz) at the original resolution and the two subscripts now denote the along-track scan number and the across-track cell position. A set of weights w_{ij} (one set for 22 GHz and another set for 37 GHz) is found such that the effective antenna pattern of the averaged T_A matches the 19-GHz antenna pattern. The weights depend on the across-track cell position because the relative location of the cells is different at the swath edge as compared to the swath center. The distance between adjacent scans and adjacent cells is approximately 25 km, and I find that it is sufficient to include only the immediately adjacent cells when doing the average. Hereafter, I drop the overbar on T_A, and it is understood that all observations are at a common spatial resolution.

3. T_B Model Parameters

At the SSM/I microwave frequencies the ocean brightness temperature T_B depends on the sea-surface temperature and roughness and on the atmospheric temperature and moisture content (vapor and cloud water). There is a strong correlation between the sea-surface roughness (i.e., capillary waves, short gravity waves, and foam) and the near-surface wind vector [Wentz, 1992], and in the T_B model I parameterize the surface roughness in terms of wind-induced surface emissivity which is a function of the near-surface wind speed W and direction ϕ. In the absence of rain the atmospheric transmittance is translucent at the SSM/I frequencies, ranging from 0.95 in dry air to 0.5 in moist tropical air. Since the SSM/I sees through the atmosphere, the total atmospheric absorption and emission can be accurately modeled in terms of the columnar water vapor V and the columnar cloud liquid water L. There is also a small dependence due to the broadening (or narrowing) of the 22 GHz water vapor line due to changes in the atmospheric pressure P. Thus the parameters of the T_B model are the following: (1) sea surface temperature T_S (kelvins); (2) effective atmospheric temperature T_E (kelvins); (3) near-surface wind speed W (meters per second); (4) near-surface wind direction ϕ; (5) columnar water vapor V (millimeters); (6) columnar liquid water L (millimeters); and (7) atmospheric pressure P (millibars). The wind is referenced to an anemometer height of 10 m. The parameters W, V, and L are retrieved from the SSM/I observations. The wind direction, in terms of the line-of-sight wind component $W \cos \phi$, is also retrieved, but certain constraints must be applied as discussed in section 4. The remaining parameters are specified via climatology and statistical relationships. I will now discuss each of these seven parameters.

The T_S dependence is weak in the 19- to 37-GHz band, with $\partial T_B / \partial T_S$ typically being about 0.3 or less. This dependence is too weak for retrieving T_S but is large enough to pro-

duce significant errors if ignored. For the results shown in this paper the Shea et al. [1990] climatology is used to specify T_S on a 2° monthly grid. Anomalies such as the El Niño-Southern Oscillation (ENSO) can produce a departure of several degrees from the climatology, and a better approach would be to specify T_S using satellite infrared observations or global circulation models.

The effective air temperature T_E corresponds to the average air temperature in the lower troposphere as defined by (16). The dependence of T_B on T_E is proportional to $1 - \tau$, where τ is the atmospheric transmittance. For moist tropical atmospheres, $\tau \approx 0.5$ at 22 GHz, and hence $\partial T_B / \partial T_E$ has a maximum value of about 0.5. Over the oceans the effective temperature widely varies from about 240 K near the ice edge to 290 K in the tropics. The analysis of radiosonde observations presented in section 8 shows that T_E is highly correlated with V and T_S. I rely on this correlation, given by (17), to specify T_E as a function of (V, T_S). Errors due to the natural variability of T_E about the (V, T_S) regression will be discussed.

Wind speed W is one of the four parameters that will be retrieved. The dependence of T_B on W is largest for h_{pol}, for which $\partial T_B / \partial W \approx 1$ K sm^{-1}. The v_{pol} derivative is considerably smaller. This polarization signature is the means by which W is retrieved. The wind direction dependence is only appreciable at winds above 5 ms^{-1}. For v_{pol}, the wind direction signal varies approximately as cos ϕ, where $\phi = 0$ corresponds to an upwind observation. For h_{pol} the dominant harmonic is cos 2ϕ. The amplitude of the signal is approximately proportional to the wind speed and reaches a peak-to-peak value of 5 K or more at high wind speeds (20 ms^{-1}). The h_{pol} wind direction signal has nearly the same spectral and polarization signature as wind speed, and hence it is not separable from wind speed. Thus it is a source of error. However, the v_{pol} wind direction signal is unique and hence can be retrieved. Since the v_{pol} dependence is cos ϕ, it is convenient to express this dependence in terms of the line-of-sight wind component W_{LS}, which equals $W \cos \phi$.

In the absence of rain, water vapor is the dominant signal at the SSM/I frequencies. Water vapor has a strong spectral signature due to the absorption line at 22.235 GHz. This strong spectral dependence makes it relatively easy to retrieve water vapor. The global variation of V is from 1 to 68 mm, and at 22V, $\partial T_B / \partial V \approx 1.5$ Kmm^{-1}. Cloud liquid water L also has a strong spectral dependence, increasing approximately as the square of frequency. This spectral signature, along with a polarization signature that is different from wind speed, provides the means to retrieve L. Typical values of L for nonrain clouds range from 0.05 to 0.20 mm (and greater), and the h_{pol} sensitivity at 37 GHz is $\partial T_B / \partial L \approx 90$ Kmm^{-1}. The columnar vapor and cloud contents are defined by

$$V = 10^{-3} \int \rho_V(h) dh \qquad (3a)$$

$$L = 10^{-3} \int \rho_L(h) dh \qquad (3b)$$

where the integral is over height h (meters) from the surface through the troposphere, and the terms ρ_V and ρ_L are the water vapor and cloud water densities (grams per cubic meter). The factor of 10^{-3} converts from units of grams per square meter to millimeters.

The remaining parameter is the effective atmospheric pressure of the water vapor column. An increase in the air pressure broadens the water vapor line and thereby increases the absorption at 19 and 37 GHz and decreases it at 22 GHz. For

example, for a pressure increase of 10 mbar, the change in the 19-, 22-, and 37-GHz vapor absorption is +0.3%, –0.9%, and +0.8%, respectively. I express the pressure dependence in terms of the following effective pressure:

$$P = 10^{-3}V^{-1}\int P(h)\rho_V(h)dh \qquad (4)$$

where the integral is from the surface through the troposphere and $P(h)$ is the air pressure (millibars) at altitude h. Globally, the water vapor column height tends to increase with increasing V, and hence P tends to decrease with increasing V. This global correlation of P versus V is accounted for in the T_B model through the statistical relationship between vapor absorption and V. However, variations in P from its typical value for a given V will cause small retrieval errors. Section 8 discusses how variations in P can be detected and how the retrieval error can be reduced.

4. SSM/I Ocean Retrieval Algorithm

The antenna temperature equation (1) is rewritten by substituting the T_B model function into the right-hand side:

$$T_{AIP} = G_{IPV} F_{IV}(W,V,L,\phi) + G_{IPH} F_{IH}(W,V,L,\phi) + G_{IPO} T_{BC} \qquad (5)$$

The model function is expressed in terms of an isotropic component $F_{IP}(W,V,L)$, $p = v$ or h, and a component that depends on wind direction ϕ.

$$F_{IV}(W,V,L,\phi) = F_{IV}(W,V,L) + \tau^2 b_V W \cos\phi \qquad (6a)$$

$$F_{IH}(W,V,L,\phi) = F_{IH}(W,V,L) + \tau^2 b_H W \cos 2\phi \qquad (6b)$$

The isotropic model function is given in section 5. The wind direction dependence of the model comes from the investigation done by *Wentz* [1992]. This investigation showed that the wind direction signal is approximately proportional to the wind speed and that the dominant harmonic for v_{pol} is cos ϕ and for h_{pol} is cos 2ϕ. The derivative of T_B with respect to a change in the sea-surface emissivity E (i.e., $\partial T_B/\partial E$) is proportional to the square of the transmittance τ. The atmospheric effect is τ^2 rather than τ because variations in the surface emissivity affect both the emitted surface radiation and the reflected atmospheric radiation. Thus treating the wind direction signal as a variation to the surface emissivity gives the factor of τ^2 in the above equations. Note that the transmittance τ is an implicit function of V, L, and frequency. Analyses of SSM/I observations [*Wentz*, 1992] and aircraft observations [*Yueh et al.*, 1995] show that the b_V and b_H coefficients do not significantly vary over the 19- to 37-GHz band. A linear fit to the SSM/I results gives $b_V = 0.12$ K sm^{-1} and $b_H = -0.09$ K sm^{-1}. The h_{pol} wind direction signal has nearly the same spectral and polarization signature as wind speed and hence is not separable from wind speed. Thus I drop the h_{pol} wind direction signal from the formulation, and it becomes a source of error. However, the v_{pol} wind direction signal is unique and hence can be retrieved.

The parameters to be retrieved are W, V, L, and line-of-sight wind $W_{LS} = W \cos\phi$. Values for the four unknowns are found by solving a system of four T_A equations for the 19V, 22V, 37V, and 37H (where V is vertical and H is horizontal) channels. At 19 and 37 GHz there are dual-polarization observations, and it is convenient (but not necessary) to transform the T_A equations into T_B equations. This cannot be done at 22 GHz because SSM/I does not have a 22 GHz, h_{pol} channel. Substituting (6) into (5) and doing the linear T_A to T_B

transformation gives

$$T_{B19V} = F_{19V}(W,V,L) + \tau_{19}^2 \ b_V W_{LS} \qquad (7a)$$

$$T_{A22V} = G_{22VV}[F_{22V}(W,V,L) + \tau_{22}^2 \ b_V W_{LS}]$$
$$+ G_{22VH}F_{22H}(W,V,L) + G_{22VO} T_{BC} \qquad (7b)$$

$$T_{B37V} = F_{37V}(W,V,L) + \tau_{37}^2 \ b_V W_{LS} \qquad (7c)$$

$$T_{B37H} = F_{37H}(W,V,L) \qquad (7d)$$

where the observation at 19 and 37 GHz is now in terms of brightness temperature, which is a linear combination of the antenna temperatures:

$$T_{BIP} = g_{IPV} T_{AIV} + g_{IPH} T_{AIH} + g_{IPO} T_{BC} \qquad (8)$$

The g coefficients come from inverting the matrix of G coefficients in (1), and their values are given by *Wentz* [1991].

The set of (7a) - (7d) is solved by first eliminating the W_{LS} unknown:

$$T_{A22V} = G_{22VV}[F_{22V}(W,V,L) + (\tau_{22}/\tau_{19})^2 \Delta T_{BV}]$$
$$+ G_{22VH}F_{22H}(W,V,L) + G_{22VO} T_{BC} \qquad (9a)$$

$$T_{B37V} = F_{37V}(W,V,L) + (\tau_{37}/\tau_{19})^2 \Delta T_{BV} \qquad (9b)$$

$$T_{B37H} = F_{37H}(W,V,L) \qquad (9c)$$

where the term ΔT_{BV} is the 19 GHz v_{pol} observation minus the isotropic model function:

$$\Delta T_{BP} = T_{B19P} - F_{19P}(W,V,L) \qquad (10)$$

where subscript P denotes polarization and equals V (vertical) or H (horizontal).

The inclusion of the fourth parameter W_{LS} introduces the term ΔT_{BV} into the retrieval equations. The ΔT_{BV} term contains both wind direction information and modeling error. When the wind is low (< 5 ms^{-1}), the wind direction signal is weak and the inclusion of ΔT_{BV} into the retrieval equations does not help the retrievals. Rather, it introduces additional noise. Furthermore, in the tropics where the atmospheric absorption is large, the modeling error increases and the wind direction signal decreases due to a lower atmospheric transmittance. The four-parameter retrieval can be optimized by applying a reduction factor γ to ΔT_{BV} that accounts for the wind-signal to modeling-error ratio. I find that the following reduction factor works well:

$$\gamma = \gamma_0 \tau_{19}^2 \Lambda(x) \qquad (11a)$$

$$x = (W - 3)/5 \qquad (11b)$$

where γ_0 equals 0.5 and 0.9 for 22 and 37 GHz, respectively, and $\Lambda(x)$ is a weighting function that smoothly goes from 0 to 1 as its argument x goes from 0 to 1.

$$\Lambda(x) = 0 \qquad\qquad x < 0 \qquad (12a)$$

$$\Lambda(x) = 3x^2 - 2x^3 \qquad 0 \le x \le 1 \qquad (12b)$$

$$\Lambda(x) = 1 \qquad\qquad x > 1 \qquad (12c)$$

For winds below 3 ms^{-1}, the γ factor eliminates the ΔT_{BV} term from the retrieval equations, thereby avoiding the problem of unnecessarily introducing additional noise when there is no need to make the wind direction correction. The τ_{19} term reduces the wind direction correction in the tropics where the

noise in ΔT_{BV} is larger due to the higher amount of water vapor.

Introducing the γ factor in (9) gives

$$T_{A22V} = G_{22VV} [F_{22V}(W,V,L) + 0.5 \, \Lambda(x) \, \tau_{22}^2 \, \Delta T_{BV}]$$
$$+ \, G_{22VH} \, F_{22H}(W,V,L) + G_{22VO} \, T_{BC} \qquad (13a)$$

$$T_{B37V} = F_{37V}(W,V,L) + 0.9 \, \Lambda(x) \, \tau_{37}^2 \, \Delta T_{BV} \qquad (13b)$$

$$T_{B37H} = F_{37H}(W,V,L) \qquad (13c)$$

These three equations are solved by assuming the equations are stepwise linear in terms of W, V, and L. This iterative procedure requires a first guess, but it should be emphasized the final solution is independent of the first guess. The following values for W, V, and L are used for the first guess: 8 ms^{-1}, 30 mm, and 0.2 mm. The analytic derivatives $\partial T_B/\partial W$, $\partial T_B/\partial V$, and $\partial T_B/\partial L$ are computed at the first-guess values. The set of equations is then treated as a linear system with slopes equal to the first guess analytic derivatives, and this set of equations is solved in the usual way using Cramer's rule. The solution gives new estimates of W, V, and L. The analytic derivatives are then recomputed at the new solution point, and the equations are again solved. This procedure is continued until the difference between the observation and the model function is less than 0.1 K for each channel. Typically, five iterations are required to reach the 0.1-K convergence level. Once W, V, and L are found, the retrieval process is completed by computing the line-of-sight wind:

$$W_{LS} = \Delta T_{BV}/(b_V \, \tau_{19}^2) \qquad (14)$$

5. Isotropic T_B Model Function

The radiative transfer equation for a nonscattering atmosphere is well known [Wentz, 1983]. The brightness temperature at the top of the atmosphere as seen by a satellite radiometer is expressed as the sum of upwelling atmospheric radiation, downwelling atmospheric radiation that is reflected upward by the sea surface, and the direct emission of the sea surface attenuated by the intervening atmosphere. These three components can be expressed as follows:

$$F(W,V,L) = T_{BU} + \tau [E T_S + (1 - E) (\Omega \, T_{BD} + \tau \, T_{BC})] \qquad (15)$$

where T_{BU} and T_{BD} are the upwelling and downwelling atmospheric brightness temperatures and τ is the transmittance through the atmosphere. E is the sea-surface emissivity, and T_{BC} is the cosmic background radiation temperature equaling 2.7 K. The Ω term accounts for the fact that a rough sea surface reflects radiation from directions other than specular as discussed below.

The upwelling and downwelling brightness temperatures are expressed in terms of effective air temperatures, T_U and T_D, defined by

$$T_U = T_{BU}/(1 - \tau) \qquad (16a)$$

$$T_D = T_{BD}/(1 - \tau) \qquad (16b)$$

T_U and T_D are very similar in value, with T_U being a few degrees colder. Note that in previous sections I simply used T_E to denote both T_U and T_D. In section 8, T_U and T_D are computed from 42,195 radiosonde flights using the complete integral formulation of the RTE. I find that T_U and T_D are highly

correlated with the radiosonde columnar water vapor V (millimeters) and the sea temperature T_S (kelvins) at the radiosonde site. The following least squares regressions are found:

$$T_D = c_0 + c_1 V + c_2 V^2 + c_3 V^3 + c_4 V^4 + c_5 (T_S - T_V) \qquad (17a)$$

$$T_U = T_D + c_6 + c_7 V \qquad (17b)$$

$$T_V = 273.16 + 0.8337 V - 3.029E{-}5 \, V^{3.33} \qquad V \le 48 \qquad (18a)$$

$$T_V = 301.16 \qquad V > 48 \qquad (18b)$$

When evaluating (17a), the expression is linearly extrapolated when V is greater than 58 mm. The regression coefficients are given in Table 1. Equations (18a) and (18b) are found by regressing the climatology sea surface temperature at the radiosonde site to V. Thus T_V represents a sea-surface temperature that is typical for water vapor V. The term $T_S - T_V$ in (17a) accounts for the fact that the effective air temperature is typically higher (lower) for the case of unusually warm (cold) water. See section 8 and Figure 2 for further discussion on T_U and T_D.

For the nonraining atmosphere the total absorption along the SSM/I viewing path is the sum of the following three components: oxygen, water vapor, and liquid cloud water. It is convenient to normalize the absorption in terms of a vertically integrated quantity rather than a viewing path integrated quantity. In this way the dependence of the absorption on incidence angle θ is separated. For incidence angles below 60° the ratio of the viewing path length through the troposphere to the height of the troposphere is simply sec θ. I let A_O, A_V, and A_L denote the vertically integrated absorption components due to oxygen, water vapor, and liquid water, respectively. The path-integrated absorptions are A_O, A_V, and A_L multiplied by sec θ. The atmospheric transmittance along the SSM/I viewing path is then given by

$$\tau = \exp[-\sec \theta \, (A_O + A_V + A_L)] \qquad (19)$$

In section 8, A_O and A_V are computed from 42,195 radiosonde flights using the complete integral formulation of the RTE. I find that A_O is nearly constant over the globe, with a small dependence on the air temperature. The following expression is the least squares regression of radiosonde A_O versus T_D:

Table 1. Model Coefficients for the Atmosphere

Parameter	19 GHz	22 GHz	37 GHz
c_0, K	240.58E+0	242.04E+0	239.55E+0
c_1, K mm^{-1}	305.96E-2	297.16E-2	248.15E-2
c_2, K mm^{-2}	−764.41E-4	−769.38E-4	−438.59E-4
c_3, K mm^{-3}	885.95E-6	931.80E-6	278.71E-6
c_4, K mm^{-4}	−40.80E-7	−44.85E-7	−3.23E-7
c_5	0.60E+0	0.20E+0	0.60E+0
c_6, K	−0.16E+0	−0.15E+0	−0.57E+0
c_7, K mm^{-1}	−2.13E-2	−7.51E-2	−2.61E-2
a_O, K	11.80E+0	13.01E+0	28.10E+0
$a_{V1, LIEBE}$, mm^{-1}	2.28E-3	6.16E-3	2.06E-3
$a_{V1, SSM/I}$, mm^{-1}	2.23E-3	6.16E-3	1.85E-3
$a_{V2, LIEBE}$, mm^{-2}	0.06E-5	1.05E-5	0.49E-5
$a_{V2, SSM/I}$, mm^{-2}	0.00E-5	0.67E-5	0.17E-5

Subscript LIEBE refers to use of the vapor absorption expression by *Liebe* [1985]. See text for details. All numbers reported in exponential format. For example, read 0.06E-5 as 0.06 x 10^{-5}, equal to 0.0000006.

$$A_O = (a_O / T_D)^{1.4} \qquad (20)$$

The vapor absorption A_V is primarily a function of V. A regression of the radiosonde A_V versus V gives the following:

$$A_V = a_{V1}V + a_{V2}V^2 \qquad (21)$$

The a_O and a_V coefficients are given in Table 1 for three SSM/I frequencies. Two sets of a_V coefficients are given. The first set, denoted by subscript LIEBE, is derived from the radiosonde data using the vapor absorption expression given by *Liebe* [1985]. In section 9 I find that the Liebe coefficients produce an erroneous correlation between the cloud water retrieval and water vapor, and hence I rederive a_{V1} and a_{V2} using collocated SSM/I and radiosonde observations. These rederived coefficients, denoted by subscript SSM/I in Table 1, are used in the retrieval algorithm, and the Liebe values are given just for comparison.

In the absence of rain the radiative transfer through the cloud droplets, which are much smaller than the radiation wavelength, is governed by Rayleigh scattering and the absorption is proportional to the columnar liquid water content L (millimeters) of the cloud [*Goldstein*, 1951]. There is also a dependence on the temperature T_L (kelvins) of the water droplets. At 37 GHz the Rayleigh absorption A_{L37} is given by

$$A_{L37} = 0.208[1 - 0.026(T_L - 283)] L \qquad (22)$$

where L is in millimeters. T_L is approximated by $(T_S + 273)/2$, which is the mean temperature between the surface and the freezing level. The temperature dependence is nearly the same at 19 and 22 GHz, and Rayleigh scattering gives the following expressions for the 19- and 22-GHz cloud absorption:

$$A_{L19} = 0.2858 A_{L37} \qquad (23a)$$

$$A_{L22} = 0.3751 A_{L37} \qquad (23b)$$

The wind dependence of the T_B model function is implicit in the emissivity E and the scattering term Ω. The emissivity is given by

$$E = E_0 + E_W \qquad (24)$$

where E_0 is the specular emissivity and E_W is the wind-induced emissivity. The specular emissivity comes from the Fresnel equation, which is a function of polarization, inci-

dence angle, and the dielectric constant of seawater. In turn, the dielectric constant is a function of frequency, water temperature, and salinity. At the SSM/I frequencies the salinity dependence is very small and it is sufficient to use a nominal value of 35 parts per thousand for seawater. *Wentz* [1992] derived the following regression for the Fresnel emissivity:

$$E_0 = (\varepsilon_0 + \varepsilon_1 t + \varepsilon_2 t^2 + \varepsilon_3 t^3 + \varepsilon_4 q + \varepsilon_5 tq + \varepsilon_6 q^2 + \varepsilon_7 t^2 q)/T_S \qquad (25)$$

where $q = \theta - 51°$ and $t = T_S - 273.16$. The above expression is valid for θ between 48° and 55°. The ε coefficients are given in Table 2 for the three SSM/I frequencies and two polarizations. These ε values are the same as derived by *Wentz* [1992], except that the h_{pol} values for ε_0, ε_1, and ε_2 have been slightly modified to remove a positive wind speed bias in cold water. I find that the cold-water wind bias is removed when the following offsets are added to ε_0, ε_1, and ε_2, respectively: 1.68, -0.2417, and 0.00639. The same offsets are applied to each frequency. The new values of ε_0, ε_1, and ε_2 are given in Table 2.

The wind-induced emissivity accounts for the change in the emissivity due to surface roughness. Surface roughness changes the local incidence angle, rotates the polarization states, and diffracts the radiation. In addition, sea foam acts as an impedance match between the air and water. These processes can be characterized by a two-scale scattering model [*Wentz*, 1975], which indicates that the wind-induced emissivity can be approximated by a monotonic function of wind speed. I use the following expression for E_W:

$$E_W = M_1 W \qquad W \le W_1 \qquad (26a)$$

$$E_W = M_1 W + 0.5 (M_2 - M_1)(W - W_1)^2/(W_2 - W_1)$$

$$W_1 < W < W_2 \qquad (26b)$$

$$E_W = M_2 W - 0.5 (M_2 - M_1)(W_2 + W_1) \qquad W \ge W_2 \qquad (26c)$$

This equation represents two linear segments connected by a quadratic spline such that the function and its first derivative in W are continuous. The spline points W_1 and W_2 are 7 and 12 ms^{-1}, respectively. The slope of the two linear segments are M_1 and M_2, respectively. The two-scale scattering model indicates that M_1 and M_2 have an incidence angle dependence and a slight sea surface temperature dependence:

$$M_J = m_J + \beta (\theta - 53) + \mu (T_S - 288) \qquad (27)$$

Table 2. Model Coefficients for the Sea Surface

Parameter	19V	19H	22V	22H	37V	37H
ε_0, K	162.53E+0	83.88E+0	166.99E+0	86.98E+0	186.31E+0	101.42E+0
ε_1	-25.70E-2	-52.22E-2	-34.08E-2	-59.52E-2	-56.37E-2	-85.88E-2
ε_2, K^{-1}	17.29E-3	18.76E-3	17.35E-3	19.38E-3	14.81E-3	20.76E-3
ε_3, K^{-2}	-11.77E-5	-9.25E-5	-10.36E-5	-8.99E-5	-2.96E-5	-7.07E-5
ε_4, K deg^{-1}	21.62E-1	-14.72E-1	21.64E-1	-15.15E-1	21.23E-1	-17.01E-1
ε_5, deg^{-1}	0.70E-2	0.21E-2	0.75E-2	0.30E-2	1.17E-2	0.55E-2
ε_6, K deg^{-2}	0.45E-1	-0.16E-1	0.45E-1	-0.16E-1	0.41E-1	-0.19E-1
ε_7, K^{-1} deg^{-1}	0.14E-4	-1.10E-4	0.02E-4	-1.17E-4	-0.71E-4	-1.27E-4
β, s m^{-1} deg^{-1}	-0.81E-4	0.81E-4	-0.87E-4	0.87E-4	-1.19E-4	1.05E-4
μ, s m^{-1} K^{-1}	0.41E-5	-0.13E-5	0.54E-5	-0.16E-5	1.25E-5	-0.29E-5
m_1, s m^{-1}	0.46E-3	3.01E-3	0.34E-3	3.20E-3	-0.09E-3	3.91E-3
m_2, s m^{-1}	3.78E-3	7.50E-3	3.48E-3	7.39E-3	2.38E-3	7.00E-3
T_B offsets, K	0.78E+0	2.10E+0	0.78E+0	---------	- 1.68E+0	0.13E+0

V and H refer to verticle and horizontal, respectively. All numbers reported in exponential format. For example, read 0.06E-5 as 0.06 x 10^{-5}, equal to 0.0000006.

where subscript J equals 1 or 2. The m_1, m_2, β, and μ coefficients are given in Table 2 for the three SSM/I frequencies and two polarizations. The values of β and μ are theoretically derived from the two-scale scattering model in which the sea surface is represented as a collection of tilted facets, with each facet acting like an independent specular surface [*Wentz*, 1975]. The values for m_1 and m_2 are found from the collocated SSM/I and buoy wind observations as discussed in section 9.

The primary component of the reflected downwelling radiation is that due to the specular reflection, i.e., radiation coming from the zenith angle that equals the incidence angle θ. The specular reflection is simply $(1 - E) T_{BD}$. However, for a rough sea surface there will be an additional component of reflected sky radiation due to the tilted surface facets reflecting radiation for other parts of the sky into the direction of SSM/I. Because the downwelling radiation T_{BD} increases as the secant of the zenith angle, the total radiation scattered from the sea surface is greater than that given by simple specular reflection. The two-scale scattering computations indicate that the total scattered radiation can be approximated by multiplying the specular reflection component by the following factor:

for v_{pol} $\qquad \Omega = 1 + 2.5\,(\sigma^2 - 68\sigma^6)\tau^3$ $\qquad$ (28a)

for h_{pol} $\qquad \Omega = 1 + 6.1\,(\sigma^2 - 68\sigma^6)\tau^2$ $\qquad$ (28b)

where σ^2 is the sea surface slope variance. The term $\sigma^2 - 68\sigma^6$ reaches a maximum at $\sigma^2 = 0.07$. For $\sigma^2 > 0.07$ the term is held at its maximum value of 0.0467. For moderately high winds (12 ms^{-1}) and a moist atmosphere (high vapor and/or heavy clouds), the scattering process increases the reflected radiation by about 1 K for v_{pol} and 5 K for h_{pol}. The accuracy of the above approximation as compared to the theoretical two-scale computation is about 0.2 K. Note that when the atmospheric absorption becomes very large (that is, τ is small), Ω tends to unity because the sky radiation for a completely opaque atmosphere is isotropic.

In the two-scale scattering model, the slope variance σ^2 depends on the observation frequency f, as well as wind speed. The ocean waves having wavelengths long compared to the radiation wavelength do not contribute to σ^2. Thus σ^2 increases with f, reaching a maximum value called the optical limit. The results of *Wilheit and Chang* [1980] and *Wentz* [1983] indicate that the optical limit is reached when $f = 37$ GHz. I use the *Cox and Munk* [1954] expression for σ^2 at 37 GHz. For 19 and 22 GHz a reduction factor is applied to the Cox and Munk expression:

$$\sigma^2 = 5.22\text{E-}3\;\xi\;W \qquad (29)$$

where ξ is the reduction factor that equals 0.688, 0.739, and 1 for 19, 22, and 37 GHz, respectively. Note the Cox and Munk wind speed was measured at a 12.5-m elevation. Hence the coefficient of 5.12E-3 in their σ^2 expression is increased by 2% to account for my wind being referenced to a 10-m elevation.

The bottom row in Table 2 is a set of five offsets that are subtracted from the T_B observations. These offsets remove the overall bias between the model T_B and the observation. The offset for 22V is subtracted from the antenna temperature rather than the brightness temperature. The offsets represent a combination of instrument and modeling absolute errors. They are quite small, which indicates SSM/I is a well cali-

brated sensor and the T_B model is quite accurate in an absolute sense. In summary, (15) through (29) and the coefficients in Tables 1 and 2 completely specify the isotropic T_B model as a function of T_S, W, V, and L.

6. Buoy Wind Data Set

The buoy wind data set is obtained from the following three sources: (1) National Data Buoy Center (NDBC), (2) Pacific Marine Environmental Laboratory (PMEL), and (3) Japanese Meteorological Association (JMA). All available buoy reports from these sources are collected for the 4-year period from 1987 through 1990. NDBC operates about 75 moored buoys and 50 C-man stations located in the northeast Pacific, in the Gulf of Mexico, in the northwest Atlantic, near Hawaii, and one off the coast of Peru. Of these I select the 42 stations that are at least 30 km from the coast. PMEL distributes the Tropical Ocean - Global Atmosphere - Tropical Atmosphere Ocean (TOGA-TAO) buoy data, which is a network of moored buoys in the equatorial Pacific. For the 1987-1990 period there are 20 TOGA-TAO mooring sites. JMA operates four buoys that are off the coast of Japan. This gives a total of 66 sites, which are shown in Figure 1.

The sampling time and interval is different for the various buoy data sets. In general, the NDBC moored buoys are sampled for 8.5 min at 1-hour intervals, and the NDBC C-man anemometers are sampled for 2 min at 1-hour intervals. The TOGA-TAO buoys take continuous measurements and report the averaged wind at various intervals (1, 2, 6, and 24 hours), depending on the buoy electronics. The JMA buoys sample for 10 min at 3-hour intervals.

For each buoy location a collocation program finds all SSM/I overpasses for which any portion of the swath is within 30 km of the buoy. A time interpolation is then done to specify the buoy wind speed W_B at the time of the SSM/I overpass. In order to accommodate the various sampling times and intervals, the following triangular weighting method is used:

$$W_B = \frac{\displaystyle\sum_{I=1}^{N} \left(P - |t_{SSMI} - t_{BI}|\right) W_{BI}}{\displaystyle\sum_{I=1}^{N} \left(P - |t_{SSMI} - t_{BI}|\right)}$$

$$\text{only for } |t_{SSMI} - t_{BI}| \le P \quad (30)$$

where W_{BI} is the Ith buoy wind taken at time t_{BI}, t_{SSMI} is the SSM/I overpass time, and P is the time interval between the buoy measurements. The summation is over all buoy observations that are within P hours of the SSM/I time. In this way the time window for the SSM/I-buoy collocation increases with the sampling time interval. However if the interval is less than 3 hours, which is the case for the NDBC buoys, then P is set to 3. Thus the minimum time window for the collocation is ± 3 hours, and the maximum time window is ± 24 hours for the PMEL daily averages. When the sampling interval is ≥ 3 hours, (30) is equivalent to a linear interpolation in time using the two buoy winds that bracket the SSM/I overpass time. For shorter sampling periods, (30) gives the average of the buoy winds within a ± 3.0-hour window, weighted according to the SSM/I-buoy time difference. This triangular weighting results in the rms value of $t_{SSMI} - t_{BI}$ having a typical value of one hour, which is commensurate with the 30-km spatial window.
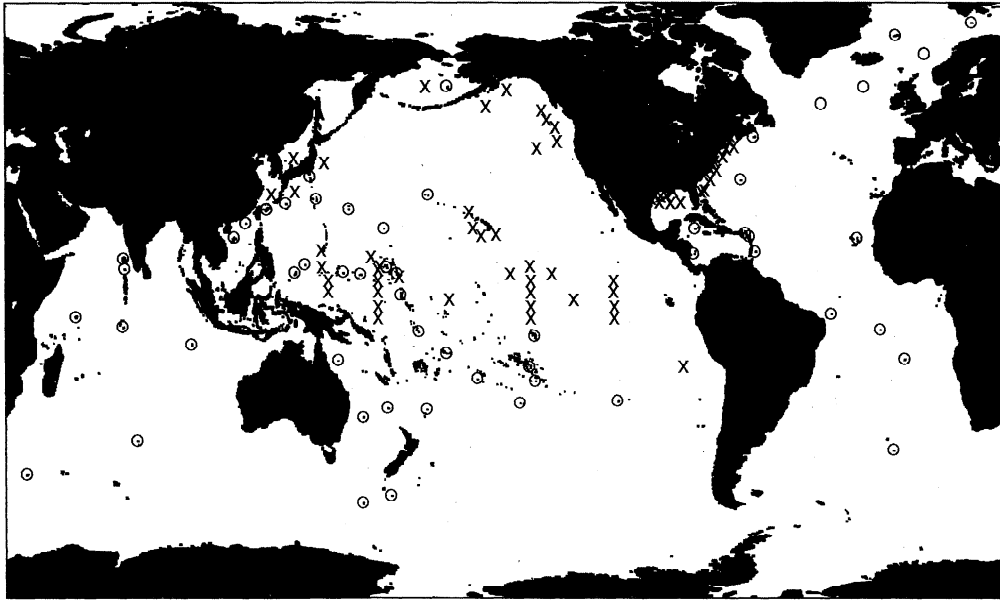
Figure 1. Locations of the buoys (crosses) and radiosonde sites (circles) used for calibrating the special sensor microwave/imager brightness temperature model and algorithm.

The buoy observations are subjected to the usual set of quality control procedures, including checks for missing data, blank fields, and out-of-bounds data. In addition, if within the specified time window the winds vary by more than 10 ms^{-1}, then the SSM/I overpass is discarded because there is probably too much variation in the wind field for an accurate satellite versus in situ comparison.

The anemometer heights H for the buoys vary. The NDBC moored buoys, in general, have H equaling 5 or 10 m, but some of the C-man stations have anemometers as high as 60 m. The PMEL anemometers are all at 3.8 m above the sea surface, and the JMA anemometers are all at 7.5 m. All buoy winds are normalized to an equivalent anemometer height of 10 m assuming a logarithmic wind profile.

$$W_{B,10m} = [\ln(10/z_0)/\ln(H/z_0)] \, W_{B,H} \qquad (31)$$

where z_0 is the surface roughness length, which equals 1.52E–4 m assuming a drag coefficient of 1.3E–3 [*Peixoto and Oort*, 1992].

7. Radiosonde Data Set

The radiosonde observations (RAOB) for the 1987 through 1990 period are obtained from the National Center for Atmospheric Research (NCAR). Since the accuracy of the SSM/I retrievals degrade when land is nearby, I select only those radiosonde sites that are on weather ships or on small islands. Figure 1 shows the location of the 55 selected sites.

For each RAOB site a collocation program finds all SSM/I overpasses for which any portion of the swath is within 60 km of the site. Most radiosonde soundings are flown at 0 UT and 1200 UT, and imposing too small of an SSM/I-RAOB time window would eliminate many sites. For example, using a 1-hour time window would select only those sites with longitudes near 90°E and 90°W since the F08 SSM/I has an ascending node time of 0600 LT. Thus I decided to use a 6-hour time window so that all sites are included. I consider that

it is more important to have a global distribution of RAOB sites than near-simultaneous observations from a few sites. When more than one RAOB observation is within ±6 hours of the SSM/I overpass time, I simply take the RAOB observation that is closest in time rather than averaging or interpolating the observations.

An objective quality control (Q/C) procedure is used to discard incomplete and anomalous soundings. Each radiosonde sounding consists of a number of levels, with each level containing a measurement of pressure, temperature, and dew point depression. If any of these three measurements is missing, the level is discarded. I define the tropospheric RAOB levels as those levels for which the pressure is greater than 180 mbar. A cutoff value of 180 mbar is used so as to include the mandatory 200-mbar level. The first step in the Q/C is to discard the sounding if the measurements for any tropospheric level are outside reasonable physical bounds. Out-of-bounds measurements occur for only 0.3% of the soundings.

The next Q/C step is to verify that the sounding contains a valid surface level reading, which is a very important level since much of the water vapor is near the surface. The RAOB data set contains a Q/C flag that identifies the surface level and indicates if it agrees with the surface report. I discard all soundings that do not have a good quality surface level. This eliminates about 8% of the total soundings. Of the remaining soundings I discard an additional 1% that have an anomalously low surface pressure that is 30 mbar below the annual average for each site.

The Q/C procedure also discards soundings that do not adequately sample the water vapor profile. I require that there be at least seven tropospheric levels and that the altitude gap between adjacent levels is always less than 3 km. Furthermore, I require that the highest tropospheric level has an air pressure less than 520 mbar and a water vapor pressure less than 0.5 mbar. About 10% of the soundings are eliminated on the basis of these criteria. The Q/C procedure also dis-

cards soundings that display large spikes in the temperature or water vapor pressure profiles. If temperature spikes greater than 6 K or vapor pressure spikes greater than 7 mbar occur, the profile is discarded. Although these spikes may be real, it is still best to exclude these soundings because the water vapor profile is probably not adequately sampled to obtain an accurate columnar vapor content. About 2% of the soundings are excluded because of large spikes in the profiles.

Those soundings passing the Q/C tests are then extrapolated from the elevation of the radiosonde station down to the sea surface. The sea-surface air pressure and vapor pressure are found by assuming they vary exponentially with height, and the sea-surface air temperature is found by assuming it varies linearly with height. The assumed exponential decay rate for vapor pressure is -0.63 km^{-1}, and the assumed air temperature lapse rate is -5.8 Kkm^{-1}. These two values are the global average values for all of the soundings. Since all but three radiosonde stations are at an elevation less that 100 m, the extrapolation down to the sea surface is a small correction that adds about 3% to the total columnar water vapor.

Another small correction is done to account for the water vapor above the tropospheric levels. For the sounding levels in the stratosphere, I do not use the RAOB water vapor measurements because they are not reliable. Instead, I simply assume an exponential decay rate of -0.63 km^{-1} and extrapolate up from the highest tropospheric level. This upward extrapolation extends to 50 km and typically adds only about 0.2% to the columnar vapor content.

The columnar water vapor V (millimeters) is found by vertically integrating the water vapor profile using the following expression:

$$V = 10^{-3} \sum_{I=0}^{N-1} (h_{I+1} - h_I)(\tfrac{1}{4}\rho_{V,I} + \tfrac{1}{4}\rho_{V,I+1} + \tfrac{1}{2}\sqrt{\rho_{V,I} \; \rho_{V,I+1}})$$

(32)

in which $\rho_{V,I}$ is the water vapor density (grams per cubic meter) for the Ith level and h_I is the altitude (meters) of the Ith level. Level 0 is sea level and level N is the last level at 50 km. To specify the vapor density ρ_V, I use the expression given by Liebe [1985] that gives ρ_V as a function of the air and dew point temperatures. The altitude h is found from the standard hydrostatic equations that give geopotential height as an integral of pressure and temperature [Peixoto and Oort, 1992]. The scaling factor of 10^{-3} converts from units of grams per square meter to millimeters. Equation (32) is a compromise between assuming ρ_V varies linearly with h and ρ_V varies exponentially with h between levels. For the case in which the relative humidity varies linearly with h, the accuracy of (32) is about 0.1%.

8. Atmospheric Coefficients and Modeling Error Derived From RAOB

The RAOB data set is used to produce simulated brightness temperatures. There are two reasons for doing this simulation. First, I need to derive expressions for the effective air temperature and for the oxygen and water vapor absorption. Second, I want to perform an error analysis in which the simulated T_B values serve as input to the retrieval algorithm. The upwelling and downwelling atmospheric brightness temperatures and the atmospheric transmittance are

computed from the standard radiative transfer equations [Wentz, 1983]:

$$T_{BU} = \int_0^H [\alpha_O(h) + \alpha_V(h)] \; T(h) \; \tau(h,H) \; \sec\theta \; dh \qquad (33)$$

$$T_{BD} = \int_0^H [\alpha_O(h) + \alpha_V(h)] \; T(h) \; \tau(0,h) \; \sec\theta \; dh \qquad (34)$$

$$\tau = \tau(0,H) \qquad (35)$$

$$\tau(h_1,h_2) = \exp\left[-\int_{h_1}^{h_2} [\alpha_O(h) + \alpha_V(h)] \; \sec\theta \; dh \right] \qquad (36)$$

The integrals in the above equations are from the sea surface $(h = 0)$ up to an altitude of $H = 50$ km, above which the atmospheric absorption is negligible. $T(h)$ is the air temperature, and $\alpha_O(h)$ and $\alpha_V(h)$ are the absorption coefficients for oxygen and water vapor. The function $\tau(h_1,h_2)$ gives the transmittance between altitudes h_1 and h_2. At the SSM/I incidence angle θ, Earth curvature effects are negligible and the differential slant path is simply given by $\sec\theta \; dh$. The absorption coefficients are computed from the RAOB measurements of pressure, temperature, and dew point depression using expressions given by Liebe [1985].
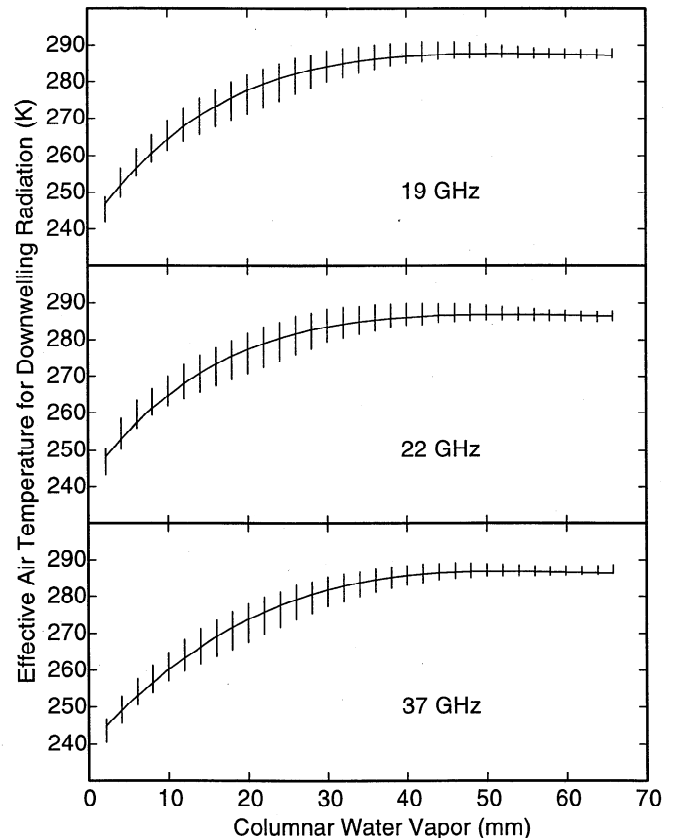
Figure 2. The effective air temperature T_D for downwelling radiation plotted versus the radiosonde observation (RAOB) columnar water vapor. The solid curves are the model value, and the vertical bars are the $\pm$ 1 standard deviation of T_D derived from radiosondes.

Table 3. Root-Mean-Square Error Budget for Retrieved Parameters

Retrieval	Atmospheric Model	Wind Direction	Radiometer Noise	Sampling Mismatch	Other	Total Observed
W, ms^{-1}	0.51	0.35	0.53	0.94	0.41	1.31
V, mm	0.81	0.21	0.43	3.68	0.74	3.87
L, mm	0.019	0.004	0.007	0	0.014	0.025
ΔT_{BV}, K	0.50	0.27	0.42	0	0.56	0.90
ΔT_{BH}, K	0.54	0.20	0.60	0	0.59	1.02

W is near-surface wind speed; V is columnar water vapor; L is columnar cloud liquid water; and T_{BV} and T_{BH} are vertical and horizontal brightness temperatures, respectively.

After applying the Q/C procedures discussed in section 7, there remains 42,195 high-quality radiosonde soundings. Equations (33) through (36) are used to compute T_{BU}, T_{BD}, and τ for this set of soundings. The effective upwelling and downwelling air temperatures, T_U and T_D, are then computed from (16). Least squares regressions, which are given by (17a) and (17b), are found that relate the air temperatures T_U and T_D to the RAOB columnar water vapor V and the sea-surface temperature T_S. Figure 2 shows T_D plotted versus V. The solid curve is the regression equation (17a), and the vertical lines show the ± 1 standard deviation of the RAOB T_D values within a 2-mm vapor bin. The corresponding figure for T_U, which is not shown, looks very similar.

I also compute the vertically integrated absorptions for oxygen and water vapor for the 42,195 soundings:

$$A_O = \int_0^H \alpha_O(h)\ dh \qquad (37)$$

$$A_V = \int_0^H \alpha_V(h)\ dh \qquad (38)$$

The least squares regressions (20) and (21) that relate A_O to T_D and A_V to V are then found. In section 9, I find that the *Liebe*[1985] regression for A_V produces an erroneous correlation between the cloud water retrieval and water vapor, and hence the coefficients in the A_V regression are rederived so as to eliminate the cloud-vapor cross talk.

Simulated ocean brightness temperatures are computed from the equations given in section 5, except that in (15), T_{BU}, T_{BD}, and τ are calculated from the RAOB profiles using (33), (34), and (35). A clear sky and a wind speed of 7 m/s are assumed. The simulated T_B values are processed by the retrieval algorithm described in section 4, and retrieved values of W, V, L, ΔT_{BV}, and ΔT_{BH} are found. Since the simulated T_B values are computed using *Liebe*'s [1985] water vapor absorptions, to be consistent in the retrieval algorithm, I use the Liebe regression for A_V (i.e., Liebe values of α_{V1} and α_{V2} in Table 1). The retrieved values are then compared with their true values to determine the algorithm performance. This simulation determines the retrieval error due to variations in the shape of the atmospheric profiles and due to the approximations inherent in the regressions for T_U, T_D, A_O, and A_V. The rms values of the retrieval errors in W, V, L, ΔT_{BV} and ΔT_{BH} are given in the first column of Table 3 for the atmospheric model error. This table contains the various error sources that contribute to the overall observed rms variations of W, V, L, ΔT_{BV} and ΔT_{BH} as will be discussed in the following sections.

An analysis reveals that ΔT_{BV} and ΔT_{BH} contain information on the effective air pressure P of the water vapor column de-

fined by (4). An increase in P broadens the water vapor line and thereby increases the absorption at 19 and 37 GHz and decreases it at 22 GHz. For example, a pressure increase of 10 mbar changes the 19-, 22-, and 37-GHz vapor absorptions by +0.3%, −0.9%, and +0.8%, respectively. Globally, the water vapor column height tends to increase with increasing V, and hence P tends to decrease with increasing V. The following simple regression that relates P (mbars) to V (millimeters) is found:

$$P = 860 - 1.15\ V \qquad (39)$$

This global correlation of P and V is absorbed in the regression (21) of A_V versus V. However, variations in P from the typical value given by (39) are not accounted for in the model,
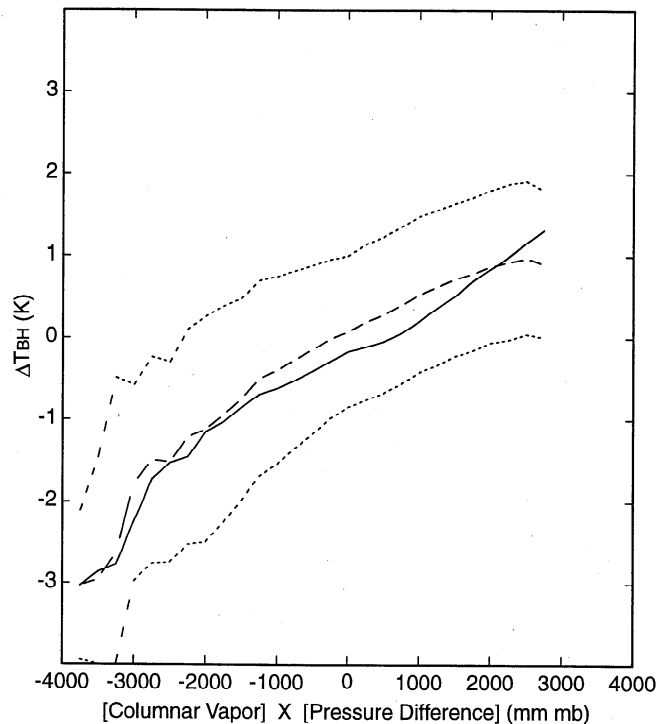
Figure 3. The T_B modeling error produced by variations in air pressure. The model error is indicated by the residual ΔT_{BH}, which is plotted versus the product of the columnar water vapor V times the air pressure variation. The solid curve comes from theoretical simulations. The long-dashed and short-dashed curves show the mean and ± 1 standard deviation envelope, respectively, of the SSM/I retrievals of ΔT_{BH}.

and these P variations show up as modeling errors in ΔT_{BV} and ΔT_{BH}. Figure 3 shows ΔT_{BH} plotted versus the product of ΔP times V, where ΔP is the difference between the effective pressure for a given RAOB sounding computed from (4) minus the typical pressure given by (39). The solid line in Figure 3 is the value of ΔT_{BH} predicted by the simulation. For unusually low pressures the true water vapor line is more narrow than that assumed by the retrieval algorithm, and hence the algorithm overcorrects for the vapor absorption at 19 and 37 GHz. This overcorrection shows up as a negative ΔT_{BH}. The curve for ΔT_{BV}, which is not shown, is similar to that for ΔT_{BH} but has about half the amplitude. This dependence of ΔT_{BH} on the effective pressure is also apparent in the actual SSM/I observations. The long-dashed curve in Figure 3 is the retrieved value of ΔT_{BH} coming from the SSM/I observations, and the short-dashed curves are the ± 1 standard deviation envelope of the retrieved ΔT_{BH}. The retrieved ΔT_{BH} closely follows the curve predicted by the simulations.

The primary effect of variations in P on the SSM/I retrievals is an error in the liquid water L due to overcorrecting or undercorrecting for the water vapor absorption at 37 GHz. This error in L can be as large as 0.1 mm for extreme case of $V\Delta P_V = -4000$ mm mbar. To reduce this error, I apply the following correction to the retrieved value $A_{L37,ret}$ of the 37-GHz absorption:

$$A_{L37,corr} = A_{L37,ret} - 0.003\ \Delta T_{BH} \qquad (40)$$

The corrected liquid water content is then found from (22). This correction is applied after the retrieval algorithm is run, and it reduces the error in L due to P by about a factor of 2. The errors in vapor and wind due to variations in P are relatively small (0.2 ms^{-1} and 0.4 mm), and no correction is made. In addition to providing a means to correct L, the information on P contained in ΔT_{BH} may have some scientific value. For example, global monthly averages of ΔT_{BH} might reveal anomalies in the shape of the water vapor profile. Research done by Schulz et al. [1993] also suggests the SSM/I observations contain useful information on the water vapor profile shape.

9. Coefficients Derived From Inverse Modeling

As discussed in section 5, some of the coefficients in the T_B model are derived from the collocated SSM/I-buoy and SSM/I-RAOB data sets. This subset of coefficients derived from SSM/I and in situ comparisons is listed in Table 4. Let the difference between the SSM/I wind minus the buoy wind be denoted by ΔW, and let the difference between the SSM/I

water vapor minus the RAOB water vapor be denoted by ΔV. The model coefficients are derived such that the following sets of conditions are satisfied: (1) The mean value of ΔW is 0 over the full range of T_S, W, V, and L. (2) The mean value of ΔV is 0 over the full range of T_S, W, V, and L. (3) The mean v_{pol} residual ΔT_{BV} is 0 over the full range of T_S, W, V, and L. (4) The mean h_{pol} residual ΔT_{BH} is 0 over the full range of T_S, W, V, and L. (5) The $L = 0$ point of liquid water histograms is centered on the steep left-hand side of the histogram and does not vary over the full range of T_S, W and V.

There are 19 conditions in all. Sets 1 through 4 each have four conditions, and set 5 has three conditions. Deriving the model coefficients in this way is called inverse modeling: the model derivation is based on the outputs of the model's inverse (i.e., the retrieval algorithm).

With respect to sets 1 through 4, the value for T_S comes from climatology [Shea et al., 1990] and the values for W, V, and L come from the SSM/I retrieval algorithm, with the following two exceptions. For set 1, W is the average of the SSM/I wind and the buoy wind, and for set 2, V is the average of the SSM/I vapor and the RAOB vapor. By doing this, the SSM/I and in situ values are given equal weight in determining the ΔW versus W and the ΔV versus V curves.

With respect to the fifth set of conditions, if the true probability density function (pdf) for L has a maximum at $L = 0$ and rapidly decays similar to an exponential pdf, then the pdf for the retrieved L has the property that its left-hand side half-power point marks the $L = 0$ point. This can be shown by adding Gaussian noise to a random deviate having an exponential pdf. Thus condition 5 requires that the left-hand side half-power point of the L pdf be at $L = 0$ for all T_S, W, and V.

Table 4 shows the principal condition that governs the derivation of each coefficient. In Table 4 the conditions are denoted in functional form. For example, the condition that ΔW is 0 over the range of T_S is denoted by $\Delta W(T_S) = 0$, and the condition that the liquid water histograms are aligned for all V is denoted by $L_0(V) = 0$. Two things should be noted. First, the derivation of a coefficient is affected not only by the principal condition given in Table 4, but also to a lesser extent by other conditions as well. Second, there are more conditions to satisfy than coefficients to determine. There are 19 conditions, and each condition represents a requirement of zero bias over the full range of a geophysical parameter. Thus the coefficient derivation problem is overdetermined, and a priori, there is no guarantee that the model will be able to accurately satisfy all conditions.

Before deriving the coefficients, the collocated SSM/I-buoy and SSM/I-RAOB data sets are subjected to a final quality control procedure. Observations near land and those

Table 4. Principal Conditions for Deriving Coefficients in T_B Model

Coefficient	Channel	Condition
α_{V1}, α_{V2}	19	$\Delta T_{BV}(V) = 0$
α_{V1}, α_{V2}	22	$\Delta V(V) = 0$
α_{V1}, α_{V2}	37	$L_0(V)=0$
m_1, m_2	19V	$\Delta T_{BV}(W) = 0$
m_1, m_2	19H	$\Delta T_{BH}(W) = 0$
m_1, m_2	22V	interpolation between 19V and 37V
m_1, m_2	22H	interpolation between 19H and 37H
m_1, m_2	37V	$L_0(W) = 0$
m_1, m_2	37H	$\Delta W(W) = 0$
ε_0, ε_1, ε_2	19H, 22H, 37H	$\Delta W(T_S) = 0$, $\Delta T_{BH}(T_S)=0$

affected by rain are discarded. If the land contamination is greater than 0.2 K, then the observation is discarded. Many observations are completely free of land contamination, and the overall effect of land should be negligible. The exclusion of near-land observations affects our selection of the collocation spatial window. For the buoys, which are mostly in the open ocean, I use a very tight window with a 30-km radius about the buoy. For the RAOBs, which are mostly on small islands, I must use a larger window of 60-km in order to avoid the island.

Observations affected by rain are also excluded. An investigation of 38 northeast Pacific storm systems [*Wentz*, 1990] indicated that when L exceeds 0.18 mm, drizzle or light rain is likely. Thus I use $L \geq 0.18$ mm as an indicator of rain. The wind speed retrieval is particularly sensitive to rain, and if rain is present in any of the seven 25-km cells that go into the T_A average given by (2), then the observation is excluded from the SSM/I-buoy data set. This excludes about 22% of the buoy observations. The water vapor retrieval is much more robust and is not seriously affected by light rain. Thus for the SSM/I-RAOB data set an observation is excluded only when $L \geq 0.5$ mm. This excludes about 4% of the observations.

After applying the Q/C procedures and space-time windows discussed in sections 6 and 7 and then excluding the near-land and rain observations, I obtain a total of 37,650 SSM/I overpasses of buoy sites and 35,108 overpasses of RAOB sites. For each overpass there are typically four to five (six to seven) high-quality SSM/I observations within a 30-(60-) km radius of the buoy (RAOB). This yields a total of 167,264 SSM/I-buoy matchups and 238,627 SSM/I-RAOB matchups.

The coefficients are then determined by varying their values until the 19 conditions listed above are generally satisfied. Previous investigations gave good initial values for the coefficients, and these initial values are adjusted via trial and error until the conditions are satisfied. In addition to determining the model coefficients, a set of five T_B offsets are found so that the global mean values for ΔW, ΔV, ΔT_{BV}, ΔT_{BH} are 0 and the global cloud histogram is properly positioned at $L = 0$. Table 2 gives these offsets for each channel, which are subtracted from the observed T_B values, except that the 22V value is subtracted from the T_A observation. The offsets represent a combination of instrument and modeling absolute errors. The offsets are quite small (1 to 2 K), which indicates that the SSM/I and the T_B model are well calibrated in an absolute sense.

The degree to which the model and algorithm satisfies the 19 conditions is shown in Figures 4 and 5. Figure 4 shows the 16 conditions relating to ΔW, ΔV, ΔT_{BV}, and ΔT_{BH}, which are plotted versus T_S, W, V, and L. The solid curve is the mean value, and the dashed curves are the $\pm$ 1 standard deviation envelope. The curves are produced by first binning the data and then computing the mean and rms statistics for each bin. An ideal algorithm would produce flat curves along the zero axes over the entire range of the four parameters. Deviations from a flat curve are a measure of systematic errors or crosstalk among the retrievals. The total rms variations for ΔW, ΔV, ΔT_{BV}, and ΔT_{BH} displayed in Figure 4 are entered into the rightmost column of Table 3. The systematic errors in ΔW, ΔV, ΔT_{BV}, and ΔT_{BH} are smaller than the rms errors. By systematic errors, I mean the deviation of the solid curves in Figure 4 from the zero baseline. The systematic errors in ΔW, ΔV, ΔT_{BV}, and ΔT_{BH} are typically 0.3 ms^{-1}, 0.6

mm, 0.3 K, and 0.3 K, respectively. There are a few instances for which the systematic error is significantly larger than these values such as the 1.7-mm dip in ΔV that occurs at V=62 mm. However, these larger systematic errors occur for bins having few observations. For example, the bin for the ΔV dip has only 1271 observations, whereas the typical bin has about 7000 observations.

The remaining three conditions are shown in Figure 5, in which the liquid water pdfs are stratified according to T_S, W, and V. Figure 5 (top) shows six histograms corresponding to 6 different ranges of SST (i.e., 0-5°C, 5-10°C, ..., 25-30°C). Figure 5 (middle and bottom) shows analogous results for wind and water vapor groupings. The peak of the pdfs is near $L = 0.025$ mm, and at $L = 0$ the pdfs are about half the peak value. I use the width of this half power point (i.e., 0.025 mm) as an indicator of the rms error in L and this value is entered into Table 3. To specify the systematic error in L, I use the alignment of the left side of the histograms. This alignment is about ±0.005 mm.

With respect to the cloud liquid water accuracy, I am assuming that the average temperature T_L of the cloud is precisely known. In the model, T_L equals the mean temperature between the surface and the freezing level. When the actual cloud temperature differs from T_L, there will be an additional error in L which can be computed according to (22). For example, an error of 4 K in T_L results in a 10% error in L.

I compare the water vapor absorption coefficients α_{V1} and α_{V2} derived herein with the values derived in section 8 using *Liebe's* [1985] expression. The two sets of values are given in Table 1. At 19 and 22 GHz, my values agree well with
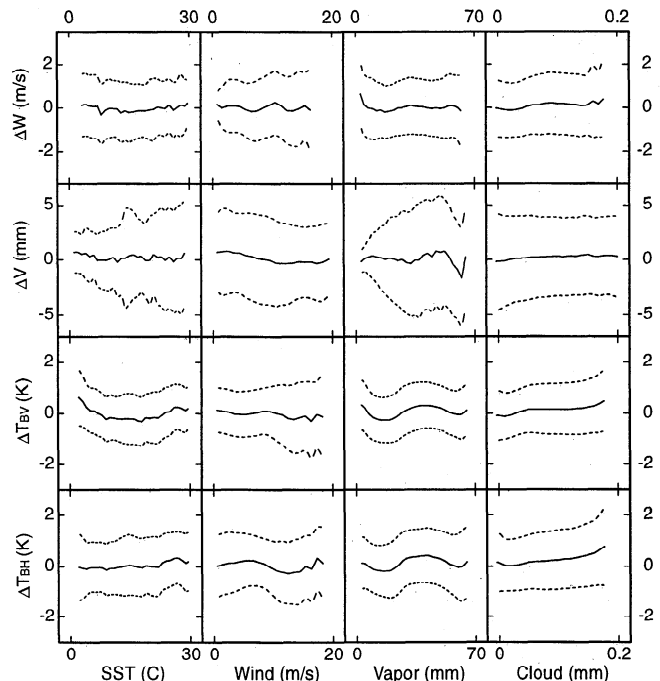
Figure 4. SSM/I retrievals for 37,650 overpasses of buoy sites and 35,108 overpasses of RAOB sites. The SSM/I minus buoy wind speed difference ΔW, the SSM/I minus RAOB vapor difference ΔV, and the v_{pol} and h_{pol} T_B residuals ΔT_{BV} and ΔT_{BH} are shown plotted versus sea-surface temperature, wind speed, columnar water vapor, and columnar cloud water. The solid lines show the mean value of the parameter, and the dashed lines show the $\pm$ 1 standard deviation.
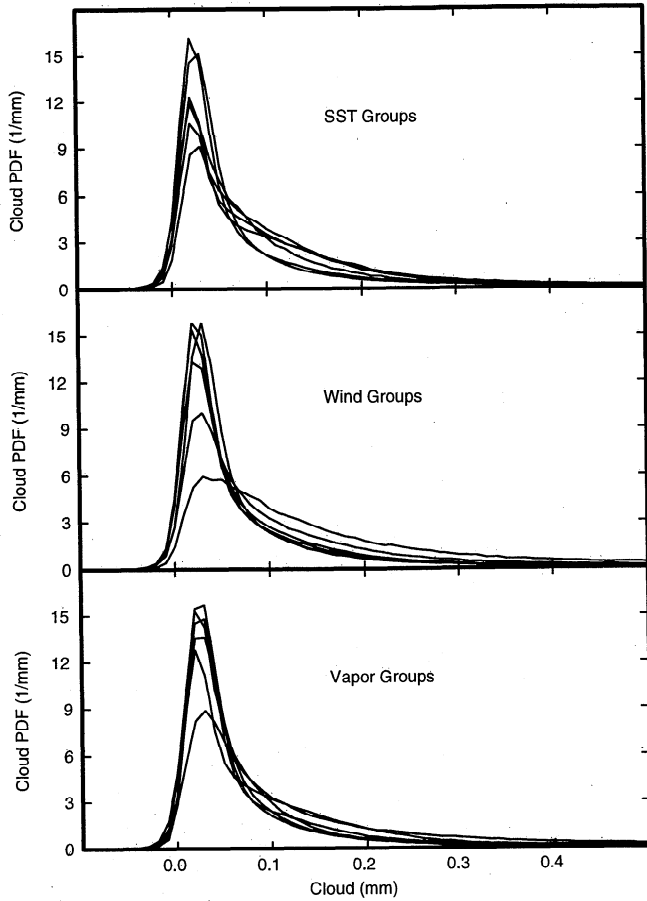
Figure 5. Probability density functions (pdfs) for liquid cloud water. The cloud pdfs are stratified according to sea-surface temperature, wind speed, and water vapor. Each curve shows the pdf for a particular stratification.

Liebe's, with the Liebe values giving an absorption that is a few percent higher. However, at 37 GHz the Liebe absorption is about 20% higher than mine. I did a test case in which the Liebe values were used in the retrieval algorithm. For this case the liquid water pdfs shown in Figure 5 for the water vapor groupings were significantly displaced, indicating an overcorrection for water vapor at 37 GHz. Most likely, the water vapor continuum used by Liebe is responsible for this problem.

To determine the sensitivity of the inverse modeling results to variations in the in situ data set, I did numerical experiments in which a subset (one half) of the in situ data is used to determine the model coefficients and the remaining one half of the data is used to test the algorithm's performance. For example, I randomly selected data for every other day. Because the data set is so large, the random division of the data into two halves has essentially no effect on the value of the model parameters nor the performance statistics. This exercise demonstrates that the calibration data set is sufficiently large so as to ensure a stable derivation.

10. Wind Direction Effects

This section discusses the retrieval of wind direction information from SSM/I. Figure 6 shows the line-of-sight wind retrieval W_{LS} plotted versus the relative wind direction ϕ for

the 37,650 SSM/I overpasses. The angle ϕ is the SSM/I look direction minus the buoy wind direction, with $\phi=0$ corresponding to an upwind observation. The four plots correspond to four different wind speed ranges. The data have been averaged into ϕ bins that are 15° in width. The long-dashed line is the mean value of the retrieved W_{LS}, and the short-dashed lines are the ± 1 standard deviation of the retrieved W_{LS}. The solid line is W_{LS} reported by the buoy, which simply equals $W_{BUOY} \cos \phi$. The mean W_{LS} agrees fairly well with the buoy value, except that the downwind minimum of the retrieved W_{LS} is more flat than that for a $\cos \phi$ function. This distortion in the shape of the curve is due to influence of the h_{pol} directional signal on the retrieval. As mentioned above, the h_{pol} signal is a source of error, and its $-\cos 2\phi$ dependence flattens the downwind minimum.

The signal-to-noise ratio (snr) for the W_{LS} retrieval is quite weak. However, if W_{LS} is averaged over sufficiently large temporal and spatial scales, then the snr is enhanced and useful information can be obtained such as monthly SSM/I wind vector maps [*Wentz*, 1992]. Also, SSM/I swath images show that at high winds the retrieved W_{LS} does show the general direction of the wind relative to the SSM/I look direction. Furthermore, if the noise in the W_{LS} retrieval is systematic such as a bias due to a regional water vapor lapse rate, then this noise can be measured (and then removed) by averaging ascending and descending orbits over the region in question. For future two-look radiometer systems that simultaneously view the ocean from both the forward and aft directions, the noise in the wind direction retrieval can be greatly reduced by simply taking the difference between the forward and aft observations. By differencing the forward and aft observations, all modeling errors associated with W, V, and L cancel, and the
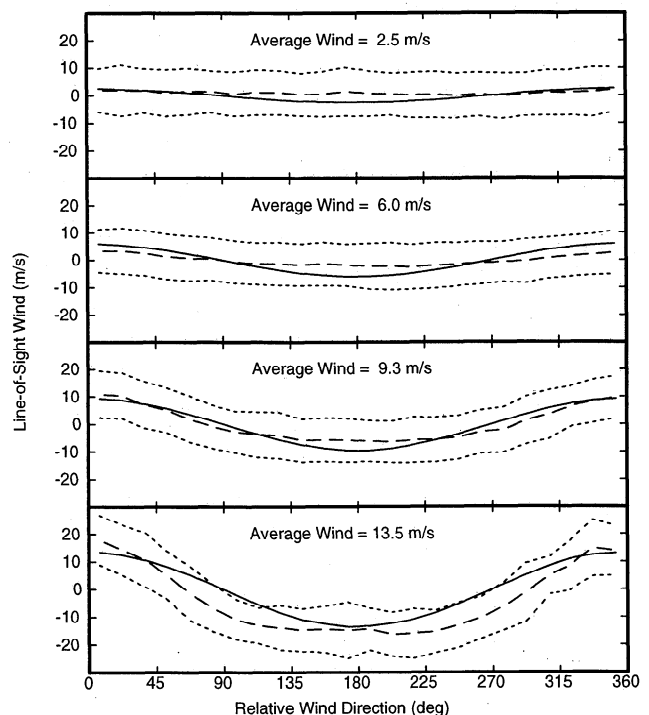

Figure 6. Retrieving the line-of-sight wind W_{LS} from SSM/I. The solid curves show the buoy W_{LS}. The long-dashed curves show the mean value of the W_{LS} retrievals, and the short-dashed curves show the ± 1 standard deviation of the W_{LS} retrievals. Results for four different wind speed groups are shown.

difference is an accurate measure of the wind direction [*Wentz*, 1992].

An important benefit of including W_{LS} in the retrieval algorithm is that it reduces the retrieval error in wind speed due to variability in the wind direction. In Figure 7 the SSM/I minus buoy wind speed difference ΔW is plotted versus ϕ. The solid curve is the mean value, and the dashed curves are the ± 1 standard deviation. To show the wind direction error more clearly, I have only included observations for which the wind is greater than 7.5 ms^{-1}. Figure 7 (top) shows the results for the algorithm described herein, and Figure 7 (bottom) shows the results when W_{LS} is left out of the retrieval by setting $\Lambda(x)$ in (13a) - (13c) to 0 for all x. As can be seen, by including W_{LS} in the retrieval, the wind error is reduced by a factor of 3. A small error still remains, reaching a maximum value of -1.0 ms^{-1} at upwind. When all observations (both low and high winds) are included in the statistics, the amplitude of the wind error due to wind direction is about 0.5 ms^{-1}, which corresponds to an rms error of 0.35 ms^{-1}. Variations in the wind direction also produce errors in the other retrievals. Computer simulations indicate the rms errors in V, L, ΔT_{BV}, and ΔT_{BH} due to wind direction are 0.21 mm, 0.004 mm, 0.27 K, and 0.20 K, respectively. These errors due to wind direction are entered into Table 3.

11. Error Analysis

In this section I fill in the two remaining entries in the error budget (i.e., Table 3). These are the error due to radiometer noise and the error due to the spatial-temporal sampling mis-
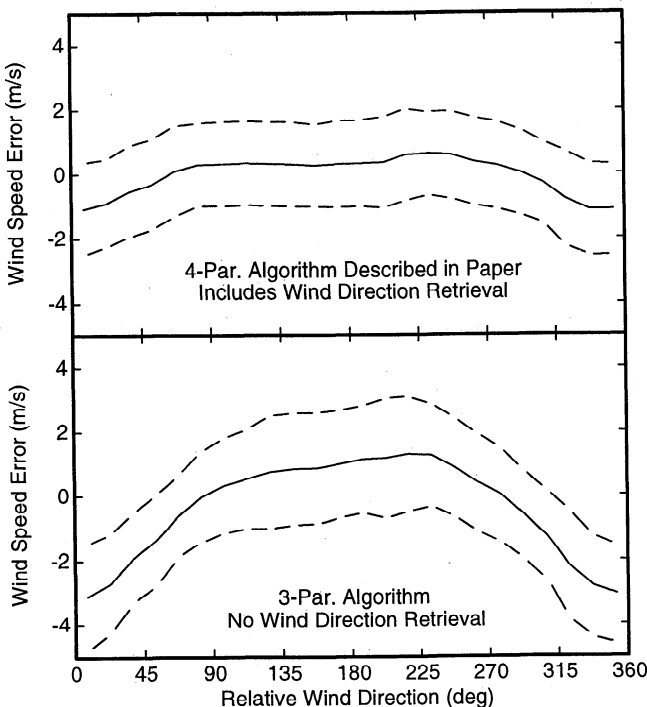
Figure 7. The error in wind speed due to wind direction variations. (top) Wind speed error versus the relative wind direction for the retrieval algorithm described herein. (bottom) Results when the algorithm does not include W_{LS}. The solid curves are the mean wind speed error, and the dashed curves are the ± 1 standard deviation of the error.

match between the SSM/I footprint and the point in situ observation. With respect to the radiometer noise, the T_A measurement error for the F08 SSM/I when averaged according to (2) is 0.4 K for 19 and 22 GHz and 0.2 K for 37 GHz. Table 3 gives the rms retrieval errors that result from just the T_A measurement noise, assuming clear skies and a 7 ms^{-1} wind.

Probably, the most difficult error component to determine is the error due to the spatial-temporal sampling error. The formulation for estimating this error is derived at the end of this section, and the results of this analysis are entered into Table 3. The sampling error is the largest component of the error budget for W and V. For wind (vapor) the sampling error accounts for 51% (90%) of the total variance of ΔW (ΔV). There is no sampling error entry in Table 3 for L, ΔT_{BV}, or ΔT_{BH} because the rms variation for these three parameters is not determined from in situ comparisons.

The four error components in Table 3 are uncorrelated, and hence the sum of their variances should equal the total observed variance. These variances are given by squaring the entries in Table 3. However, I find total observed variance is slightly greater than the sum of its components. This indicates that there is a residual error yet to be explained. This residual error is entered into Table 3 under the column entitled "other." Part of this residual error is probably due to the sea-surface modeling error. The correlation between the rough surface emissivity and the wind speed is not perfect, and this will introduce error. Biases in the in situ observations from one site to another will introduce additional error. In addition, any error in specifying the sampling error will show up in the residual error. This is particularly a problem for water vapor, for which the sampling error dominates the statistics.

I conclude this section by deriving expressions for the spatial-temporal sampling error. To estimate the SSM/I versus buoy wind sampling error, I assume the wind field has a linear gradient in space and is advecting in time. I let the x axis be in the direction of the spatial gradient, and I let v be the velocity of the advection. Then the wind at position x and time t is

$$W(x,t) = W_0 + g\,(x - v\,t \cos \varphi) + \varepsilon \qquad (41)$$

where g is the gradient (meters per second per kilometer) and φ is the angle of advection relative to the x axes. I assume an average advection speed of $v = 28.8$ kmh^{-1} (8 ms^{-1}). I have included a random wind component ε. When averaged over spatial scales equal to the SSM/I footprint (i.e., 50 km), the mean of ε is 0 and its variance, denoted by $<\varepsilon^2>$, is independent of position and time. Thus the second term in (41) accounts for variations in the wind field on spatial scales equaling the SSM/I footprint dimension, and the third term accounts for wind variation on the smaller spatial scales within the footprint. I let the buoy observation be at $x = 0$, $t = 0$:

$$W_B = W_0 + \varepsilon \qquad (42)$$

The SSM/I observation time is t, and the footprint center is at position $x = r \cos \psi$ and $y = r \sin \psi$, where r is the radial distance from the buoy to the footprint center. Averaging $W(x,t)$ over the footprint give the SSM/I wind speed:

$$W_S = W_0 + g\,(r \cos \psi - v\,t \cos \varphi) \qquad (43)$$

I now consider an ensemble of SSM/I observations over buoy sites. For this ensemble the distribution of angles ψ and φ will be fairly uniform over 0 to 2π. I let $\Delta W = W_S - W_B$ and

find the ensemble average of ΔW^2 to be

$$\left\langle \Delta W^2 \right\rangle = \tfrac{1}{2} g^2 R^2 + \left\langle \varepsilon^2 \right\rangle \qquad (44)$$

$$R^2 = \left\langle r^2 + v^2 t^2 \right\rangle \qquad (45)$$

For the buoy comparisons the spatial window of 30 km and the triangular time weighting method given by (30) results in $R = 36$ km. Thus the spatial-temporal sampling error can be estimated from (44), if I have values for the gradient g and the interfootprint spatial variability $\left\langle \varepsilon^2 \right\rangle$.

To obtain an estimate of g, I use the wind speed spatial variability observed by SSM/I. According to (43), the wind speed difference between two neighboring SSM/I footprints is simply $\Delta W_S = g \, r \cos \psi$, where r is now the radial distance between the footprints. Taking the ensemble average of ΔW_S^2 over many observations separated by a distance r gives

$$\sqrt{\left\langle \Delta W_S^2 \right\rangle} = g \, r / \sqrt{2} \qquad (46)$$

Figure 8 shows the rms value of ΔW_S derived from SSM/I plotted versus r for three wind speeds. As expected, the spatial variability increases with wind speed, and for the higher values of r the curves in Figure 8 tend to flatten out as they approach the decorrelation length for winds on the ocean. As discussed above, the SSM/I winds contain errors due to the random radiometer noise and the systematic T_B model error. For nearby cells I expect that the systematic error for the two cells will be nearly the same and hence will not be a factor in the wind speed difference. However, the radiometer noise is uncorrelated and will contribute to the rms wind difference between cells. Thus, in Figure 8, I have subtracted, in a root-mean-square sense, the radiometer noise component. I do not use the 30-km bin because its value is most sensitive to the
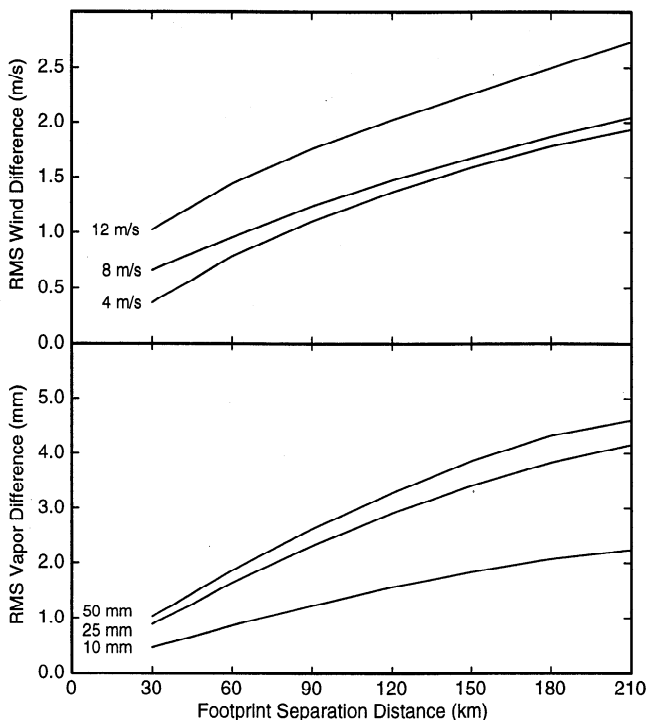
Figure 8. The rms difference of SSM/I retrievals of wind speed and water vapor for neighboring footprints. The three curves in each plot show the results for low, medium, and high values of wind and vapor.

specification of radiometer noise and the two 50-km observations overlap and hence are not independent. Rather, I use the 60-km separation distance to specify g. The curve for $W = 8$ ms^{-1} at $r = 60$ km gives a value of 0.95 ms^{-1} for the rms wind difference. Substituting this value in (46) gives a value of 0.022 ms^{-1}km^{-1} for g.

To obtain an estimate for $\left\langle \varepsilon^2 \right\rangle$, I look at the wind speed temporal variability observed by the buoys. According to (41), the wind difference between observations for the same buoy but at different times is

$$\Delta W_B = g \, v \, t \cos \varphi + \varepsilon_t - \varepsilon_0 \qquad (47)$$

where t is now the time separation between the buoy observations and ε_0 and ε_t are the random wind components at times 0 and t, respectively. Taking the ensemble average of ΔW_B^2 over many observations separated in time by t gives

$$\left\langle \Delta W_B^2 \right\rangle = \tfrac{1}{2} g^2 \left\langle v^2 t^2 \right\rangle + 2 \left\langle \varepsilon^2 \right\rangle \qquad (48)$$

The rms value of ΔW_B is found from the buoy data set to be 1.17 ms^{-1} for a $t = 1$ hour time separation. Assuming $v = 28.8$ kmh^{-1} and using the g value found above gives a value of 0.76 ms^{-1} for $\left\langle \varepsilon^2 \right\rangle^{1/2}$. Using (44), I can now estimate the rms value of the SSM/I minus buoy wind difference due to the spatial-temporal sampling error. The value is $\left\langle \Delta W^2 \right\rangle^{1/2} = 0.94$ ms^{-1}. These results are very similar to the wind spatial variability statistics reported by Monaldo [1988].

The sampling error for the RAOB comparisons is calculated in the same way. For the RAOB comparisons the space-time window of 60 km and 6 hours results in a value of $R = 122$ km. Figure 8 shows the rms vapor difference for neighboring SSM/I cells plotted versus the separation distance. For the RAOBs the smallest time interval between measurements at a given site is 6 hours, and the rms difference for the 6-hour interval is 4.8 mm. To be consistent with this time separation of 6 hours, I use the spatial gradient g that corresponds to a 180-km separation distance when computing $\left\langle \varepsilon^2 \right\rangle^{1/2}$ from (48). Then when computing the RAOB-SSM/I sampling error from (44), I use the spatial gradient that corresponds to the RAOB-SSM/I separation distance of 122 km. For $V = 25$ mm, which is the average value for the RAOB data set, I obtain a value of $g = 0.0343$ and 0.0301 mmkm^{-1} for $r = 120$ and 180 km, respectively. I find $\left\langle \varepsilon^2 \right\rangle^{1/2}$ to be 2.18 mm and the RAOB-SSM/I sampling error to be 3.68 mm.

12. Conclusions

In the absence of rain, the SSM/I T_B observations of the ocean can be modeled to a rms accuracy between 0.5 and 1 K. The model's inverse provides wind, vapor, and cloud water retrievals with an rms accuracy of 0.9 ms^{-1}, 1.2 mm, and 0.025 mm, respectively. These values are found from Table 3 by excluding the spatial-temporal sampling error, which is not part of the SSM/I retrieval accuracy. The cloud water accuracy assumes that the cloud water temperature is precisely known. The error in specifying the cloud temperature will introduce an additional 10% error in the cloud water retrieval. The spatial resolution for these accuracies is 50 km. Averaging the observations over larger spatial scales (>100 km) removes the radiometer noise component from the error budget and will improve the rms accuracies by about 20%. As compared to the rms errors, the systematic errors in the retrievals are found to be quite small, typically being 0.3 ms^{-1}, 0.6 mm, and 0.005 mm for W, V, and L, respectively. The one excep-

tion is the systematic error in wind speed of -1.0 ms^{-1} that occurs for observations within $\pm20°$ of upwind.

The algorithm places no restrictions on the retrieval ranges for W, V, and L, and the retrieved quantities cover the entire range of natural variability. Out of the 37,650 buoys, only 2 reported winds above 20 ms^{-1}. This indicates the natural variability of the wind speed for no-rain areas when averaged over a 56-km area is 0 to 20 ms^{-1}. Higher winds do occur, but nearly always, some rain is within the 56-km area. The natural variability of water vapor is from 0 to 70 mm, and the algorithm is capable of doing retrievals over this full range.

The inclusion of the line-of-sight wind W_{LS} in the retrieval significantly reduces the error in wind speed due to wind direction variations. The wind error for upwind observations is reduced from -3.0 to -1.0 ms^{-1}. Furthermore, although the signal-to-noise ratio of W_{LS} is small, there is the potential of obtaining scientifically useful information on wind direction from SSM/I for cases of high winds and when doing large-scale averages.

In addition to providing a very precise estimate of the columnar water vapor, the SSM/I observations also contain some information on the effective pressure of the water vapor profile. This information may be of some use in specifying the vertical distribution of water vapor.

These results indicate that the current model is a very accurate representation of the 19- to 37- GHz microwave emission from the ocean and intervening nonraining atmosphere. The model accounts for nearly all of the observed variation in the brightness temperature over the world's oceans. I view the T_B ocean model and associated algorithm as essentially complete and do not expect any significant future improvements in either the model or retrieval accuracies, with two caveats. First, the inclusion of additional channels such as the SSM/I 85-GHz channel or the 7- and 10-GHz channels planned for future radiometer systems may improve retrieval accuracies. Second, the current no-rain algorithm needs to be extended to include rain. The development of an all-weather ocean algorithm for SSM/I is the primary focus of my current research.

Thus far, the algorithm has been used to produce geophysical products from the F08, F10, F11, and F13 satellites. In producing this 10-year data set, I have cross-calibrated the four SSM/Is. The cross-calibration is done at the T_A level. The T_A values are first normalized to a constant incidence angle of 53.3° and are then collocated and compared. Orbit crossover points for a 1-year period are used to avoid diurnal variations. I find that the SSM/Is are very well calibrated, exhibiting satellite-to-satellite T_A differences of the order of 0.5 K. The appropriate T_A offsets are applied to F10, F11, and F13 so that the T_A values match F08. I estimated that the accuracy of this cross-calibration procedure is about 0.1 K. Once the T_A offsets are applied, the identical algorithm can be used to process data from all SSM/Is. The SSM/Is fly in slightly different orbits, particularly F10. However, the only effect that the orbit geometry has on the retrieval algorithm is through the incidence angle, which can vary by $\pm0.75°$ between satellites and within an orbit. Since incidence angle is an input parameter for the T_B model, the retrievals are not affected by incidence angle variations. The 1987-1996 SSM/I ocean products can be obtained through Remote Sensing Systems.

References

Cox, C.S., and W.H. Munk, Measurement of the roughness of the sea surface from photographs of the sun's glitter, *J. Opt. Soc. Am., 44*, 838-850, 1954.

Eisberg, R.M., *Fundamentals of Modern Physics,* John Wiley, New York, 1961.

Goldstein, H., Attenuation by condensed water, in *Propagation of Short Radio Waves, MIT Radiat. Lab. Ser., vol. 13,* McGraw-Hill, New York, 1951.

Hollinger, J., R. Lo, G. Poe, R. Savage, and J. Pierce, Special Sensor Microwave/Imager user's guide, technical report, 120 pp, Nav. Res. Lab., Washington, D.C., 1987.

Liebe, H.J., An updated model for millimeter wave propagation in moist air, *Radio Sci., 20,* 1069-1089, 1985.

Monaldo, F. M., Expected differences between buoy and radar altimeter estimates of wind speed and significant wave height and their implications on buoy-altimeter comparisons, *J. Geophys. Res., 93,* 2285-2302, 1988.

Peixoto, J.P., and A.H. Oort, *Physics of Climate,* Am. Inst. of Phys., College Park, Md., 1992.

Schulz, J., P. Schluessel, and H. Grassl, Water vapour in the atmospheric boundary layer over oceans from SSM/I measurements, *Int. J. Remote Sens. 14,* 2773-2789, 1993.

Shea, D.J., K.E. Trenberth, and R.W. Reynolds, A global monthly sea surface temperature climatology, *NCAR Tech. Note 345,* 167 pp., Nat. Cent. for Atmos. Res., Boulder, Colo., 1990.

Wentz, F.J., A two-scale scattering model for foam-free sea microwave brightness temperatures, *J. Geophys. Res., 80,* 3441-3446, 1975.

Wentz, F.J., A model function for ocean microwave brightness temperatures, *J. Geophys. Res. 88,* 1892-1908, 1983.

Wentz, F.J., SBIR phase II report: West coast storm forecasting with SSM/I, *RSS Tech. Rep. 033190,* 378 pp., Remote Sens. Syst., Santa Rosa, Calif., 1990.

Wentz, F.J., User's manual: SSM/I antenna temperature tapes, revision 1, *RSS Tech. Rep. 120191,* 69 pp., Remote Sens. Syst., Santa Rosa, Calif., 1991.

Wentz, F.J., Measurement of oceanic wind vector using satellite microwave radiometers, *IEEE Trans. Geosci. Remote Sens., 30,* 960-972, 1992.

Wilheit, T.T., and A.T.C. Chang, An algorithm for retrieval of ocean surface and atmospheric parameters from the observations of the Scanning Multichannel Microwave Radiometer (SMMR), *Radio Sci. 15,* 525-544, 1980.

Yueh, S.H., W.J. Wilson, F.K. Li, W.B. Ricketts, and S. V. Nghiem, Polarimetric measurements of sea surface brightness temperatures using an aircraft K-band radiometer, *IEEE Trans. Geosci. Remote Sens. 33,* 85-92, 1995.

F.J. Wentz, Remote Sensing Systems, 1101 College Avenue, Suite 220, Santa Rosa, CA 95494. (email: wentz@remss.com)